

# Boosting Iron-Ion Battery Performance with Porous Carbon Aerogel as High-Rate Charge/Discharge Cathode

Jitendra Kumar Yadav, Anant Prakash Pandey, Bharti Rani, Priyanka Saini, and Ambesh Dixit\*

Rechargeable Iron-ion batteries (IIBs) are emerging as a sustainable alternative to conventional rechargeable batteries; however, their cathode development is hindered by sluggish Fe-ion diffusion, limited conductivity, and interfacial instability. Addressing these challenges requires designing cathode materials with high conductivity, large surface area, and stable electrochemical interfaces. This work explores carbon aerogel (CA)-based cathodes to overcome these limitations and enhance Fe-ion storage performance. Highly porous CA, used as the cathode material, is synthesized using the sol-gel process and confirmed using transmission electron microscopy, field emission scanning electron microscopy, X-ray diffraction, and Brunauer–Emmett–Teller measurements. Detailed cyclic voltammetry is investigated at different scan rates to understand the characteristics of the Fe-ion storage in CA hosts during cycling. The galvanostatic

charging-discharging (GCD) is determined at various current densities, showing a high discharge capacity of  $\approx 150 \text{ mAh g}^{-1}$  and  $\approx 45 \text{ mAh g}^{-1}$  at  $35 \text{ mA g}^{-1}$  and  $1000 \text{ mA g}^{-1}$  discharge current densities, respectively. The capacity retention is more than  $\approx 60\%$ , with more than 85% Coulombic efficiency (CE) after 750 cycles at  $1000 \text{ mA g}^{-1}$ , and fast charge-discharge characteristics of  $\approx 18\text{C}$  rate. The galvanostatic intermittent titration technique (GITT) measurements are also performed to check the diffusion characteristics of the Fe-ion during charging and discharging. A digital clock and 5V light-emitting diode are connected to CA-based Fe-ion coin cells to demonstrate the potential of IIBs. A detailed electrochemical impedance spectroscopy and postmortem measurements before and after the GCD cycling suggest a slight degradation of electrochemical performance, which is attributed to the oxidation of the anode during cycling.

## 1. Introduction

Energy storage devices play a critical role in bridging the gap between energy production and demand by storing excess energy when available and releasing it on need.<sup>[1,2]</sup> These offer high energy density, power density, and efficiency, making them useful for stationary and mobile applications.<sup>[3,4]</sup> These electrochemical storage systems, especially batteries and supercapacitors, have undergone significant advancements in recent years, leading to cost reductions and improved performance, further enhancing their attractiveness for widespread deployment.<sup>[5–7]</sup> Li-ion batteries (LIBs) have been the most explored electrochemical energy storage system in the last four decades after their commercialization in 1991. The advantages of LIBs include high energy density, lightweight design, and long cycle life. They are

ideal for powering various devices, from portable electronic devices to electric vehicles. Their compact size and versatility enable seamless integration into multiple applications, providing portable and reliable energy storage solutions.<sup>[8–11]</sup> However, LIBs have several drawbacks, such as cost, safety, environmental friendliness, toxicity, and availability.<sup>[12–15]</sup>

Due to the similar chemistry of sodium as lithium, sodium-ion batteries have also been explored widely. The sodium-ion batteries offer potential advantages such as abundant sodium resources and enhanced safety compared to lithium-ion batteries.<sup>[16–18]</sup> However, they currently suffer from lower energy density and sluggish ion dynamics, limiting their widespread adoption for practical applications.<sup>[19,20]</sup> Due to these limiting factors for the Li/Na-ion batteries, the multivalent metal ion rechargeable batteries (MvMIBs) are gaining attention. MvMIBs utilize metal ions such as calcium, aluminum, zinc, iron, magnesium, copper, etc., to store and release energy. These MvMIBs offer the potential for higher energy densities and lower costs due to their relative abundance.<sup>[21–24]</sup> However, challenges remain in developing suitable host electrode materials and electrolytes that can efficiently intercalate and deintercalate multivalent ions (e.g.,  $\text{Mg}^{2+}$ ,  $\text{Al}^{3+}$ ,  $\text{Zn}^{2+}$ ,  $\text{Cu}^{2+}$ , etc.).<sup>[25,26]</sup>

Aluminum-ion batteries are challenged by limited cathode material compatibility, sluggish  $\text{Al}^{3+}$  ion diffusion, and electrolyte corrosion issues that restrict capacity and cycle stability.<sup>[27]</sup> Copper-ion batteries face challenges such as limited cycle life due to copper dendrite formation, sluggish ion diffusion in solid electrodes, and corrosion or dissolution of copper in aqueous

J. K. Yadav, A. P. Pandey, B. Rani, P. Saini, A. Dixit  
Advanced Materials and Devices Laboratory  
Department of Physics  
Indian Institute of Technology Jodhpur  
Jodhpur  
342030, India  
E-mail: ambesh@iitj.ac.in

A. Dixit  
Rishabh Centre for Research Innovation in Clean Energy  
Indian Institute of Technology  
Jodhpur 342030, India

 Supporting information for this article is available on the WWW under <https://doi.org/10.1002/batt.202500355>

electrolytes, leading to capacity fade.<sup>[28]</sup> Zinc-ion batteries suffer from zinc dendrite growth, hydrogen evolution in aqueous systems, and poor long-term stability due to cathode dissolution and volume changes, which degrade performance over cycles. Research efforts are underway to overcome these obstacles and unlock the full potential of multivalent metal ions, along with metal-air batteries for various applications, including electric vehicles and grid-scale energy storage, contributing to a more sustainable and resilient energy future<sup>[29–32]</sup>

Fe-ion batteries have gained popularity among MvMIBs due to several factors. Iron is the second most abundant and cost-effective (cheapest metal in terms of cost) with high volumetric energy density, making it an attractive option for large-scale energy storage applications.<sup>[33]</sup> Iron metal anode-based batteries exhibit enhanced safety characteristics and environmental sustainability compared to other battery chemistries.<sup>[34–40]</sup> Iron metal offers higher energy densities (gravimetric energy density 960 mA h g<sup>-1</sup> and volumetric energy density 7557 mA h cm<sup>-3</sup>) and redox potential (−0.44 vs. SHE), which is higher than various multivalent metal anodes, including zinc.<sup>[41]</sup> Recently, Ji's group first reported the aqueous Fe-ion batteries with various cathode materials (e.g., IPB, VOPO<sub>4</sub>) and confirmed the intercalation of the Fe<sup>2+</sup> ions during the cycling.<sup>[42,43]</sup> A-MAD research group and Ramaprabhu et al. confirmed the intercalation of Fe<sup>2+</sup> ions in V<sub>2</sub>O<sub>5</sub> and the g-C<sub>3</sub>N<sub>4</sub> cathode materials for the nonaqueous Fe-ion batteries, respectively.<sup>[44,45]</sup> Predominantly, aqueous rechargeable Fe-ion batteries are explored. Yet, there are several issues, such as iron anode corrosion in the aqueous electrolyte, less operating voltage window, and the requirement for an inert atmosphere to fabricate these batteries. Suitable electrode host materials are also challenging for rechargeable iron-ion batteries, providing an efficient intercalation/deintercalation process during cycling.<sup>[46–48]</sup> Various metal-oxide and phosphates, sulfur, PANI, etc., are explored as cathode materials, but each has pros and cons.<sup>[49–52]</sup> Developing a suitable cathode material is still challenging for Fe-ion batteries.

Carbon materials were also explored as the electrode materials due to their exceptional electrical conductivity, chemical stability, and tunable porosity. With their interconnected micro- and mesoporous networks, porous carbon materials serve as dynamic cathode hosts in MvMIBs, bridging the gap between high-capacity storage and long-term stability. Their high electrical conductivity facilitates easier electron transport.<sup>[53]</sup> Chai et al. reported that carbon foam as the cathode for an iron battery in aqueous electrolyte, showing a high CE.<sup>[54]</sup> The N-doped porous carbon was also explored in aqueous medium.<sup>[55]</sup> In this scenario, we developed a carbon aerogel-based cathode because of its unique properties, including very high surface area due to its porous structure, lightweight design, and high electrical conductivity, which makes it a suitable cathode for Fe-ion batteries. CA is widely used for hydrogen and energy storage applications, especially supercapacitors and rechargeable batteries.<sup>[56,57]</sup> In this paper, rechargeable nonaqueous Fe-ion batteries were developed using a CA cathode, synthesized via the sol-gel technique followed by carbonization. The complete coin cell assemblies were fabricated using an MS anode and a nonaqueous electrolyte. Cyclic voltammetry (CV)

measurements were carried out at different scan rates to analyze the redox mechanism. The GCD characteristics were measured at various current rates to estimate the specific capacity, capacity retention, and rate capability. The observed high specific capacity is ≈150 and ≈45 mA h g<sup>-1</sup> at 35 and 1000 mA g<sup>-1</sup>, respectively. The capacity retention is around 60% after 750 cycles with fast charge-discharge characteristics of ≈18C rate. To understand the performance degradation, electrochemical impedance spectroscopy (EIS) and postmortem (*ex situ*) measurements were carried out and analyzed before and after the GCD cycling. The observed capacity degradation is attributed to the solid electrolyte interface (SEI) formation during cycling at the anode. A demonstration was also performed by lighting a 5V LED containing fan-shaped gadgets and running a digital clock.

## 2. Experimental Section

### 2.1. Synthesis of the Carbon Aerogel

The initial step in synthesizing CA involves the preparation of a hydrogel through the sol-gel polymerization process. The CA was then synthesized by annealing the hydrogel in an argon atmosphere at high temperatures, and a complete schematic of the synthesis is shown in Figure 1a. In hydrogel synthesis, resorcinol (R, Qualigen) and formaldehyde (F, Qualigen) were dissolved in a 1:2 mol ratio in 14 ml DI water. A base catalyst (C), sodium carbonate (99.5%, Sigma-Aldrich), was added in a mole ratio of C = 0.002 R. The solution was stirred for 15–20 min and kept in a hot air oven for 72 hr at 85 °C. After three days, the hydrogel was formed, depicted in Figure 1a, and was dried under ambient conditions by undergoing acetone exchange for three days in each 24 hr. Finally, the CA was produced by carbonizing the hydrogel in an argon atmosphere at a temperature of 850 °C.<sup>[58]</sup> The final blackish outcome was the CA, which was used further in slurry preparation.

### 2.2. Electrodes and Electrolyte Preparation

A slurry was made to prepare the CA electrode by following the steps shown in Figure 1b. The slurry contains CA as the active cathode material, PVDF (Polyvinylidene Fluoride, AlfaAesar) as a binder, and carbon black (99.9%, AlfaAesar) as a conductive material in a fraction of 80:10:10. The overall combined powder was ground in mortar-paste until it became very fine. The fine powder was added to the solvent of N-methyl pyrrolidone (NMP, ACS reagent, ≥99.0% Sigma-Aldrich) and stirred for 24 hr. The resulting slurry was applied onto stainless steel (SS) spacers using the drop-cast method. After coating the spacers, it is dried for 2 hr at 80 °C. Once the drying process is complete, the CA electrode is ready to use in the coin cell. A mild steel metal sheet with a thickness of 0.4 mm is used as the anode without a current collector. 1 M iron(II) perchlorate hydrate (98%, Sigma-Aldrich) salt was dissolved in the tetra-ethylene glycol dimethyl ether (TEGDME, ≥99%, Sigma-Aldrich) and stirred for 24 hr before use as an electrolyte in the coin cell.

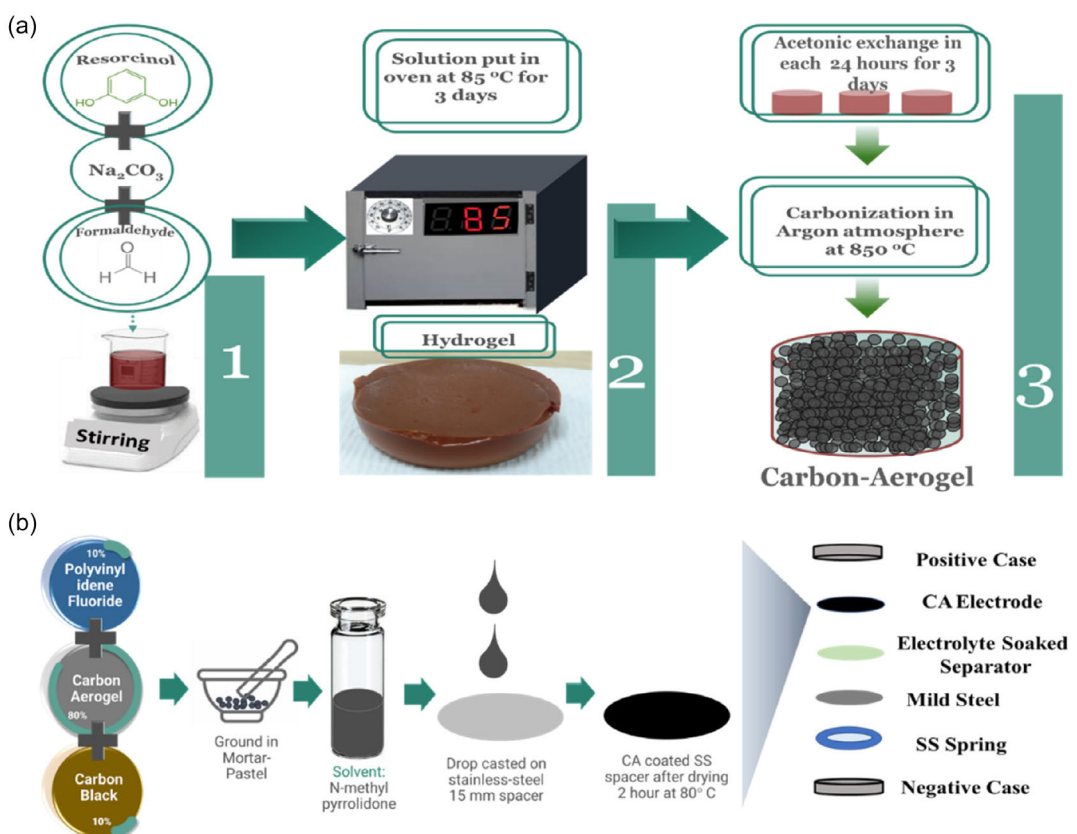


**Figure 1.** a) Synthesis of the CA using the sol–gel polymerization method, followed by the carbonization. b) Schematic for the electrode slurry preparation, along with coin cell fabrication.

### 2.3. Coin Cell Fabrication

The required components of the coin cell assembly are shown in Figure 1b, including the negative case, SS spring, separator, mild steel, and positive case. First, an SS spring and mild steel are inserted in a negative case to assemble the coin cell. Next, the electrolyte-soaked separator (Whatman filter paper, Cytiva) is placed on top of the mild steel anode, followed by a CA electrode as the cathode coated on the SS spacer. Finally, the positive case is placed over the cathode to complete the cell assembly. The cell assembly is then crimped using a hydraulic machine at 1000psi pressure for 10 s. The prepared coin cell is used for various electrochemical characterizations.

### 2.4. Characterization

The Miniflex-II X-ray diffraction (XRD) system was used to perform the crystallographic studies on the synthesized electrode materials. The pre- and postmortem XRD were investigated using the Malvern PANalytical Empyrean model. The surface area of the CA was calculated using Brunauer–Emmett–Teller (BET) (Autosorb Quanta Chrome, iQ3 model) surface area analysis. Field emission scanning electron microscopy (FESEM) (Thermo Scientific Apreo 2S) was performed to check the electrode morphology. Scanning electron microscopy (SEM) (Carl Zeiss EVO 18) system

to check the electrode morphology after the complete cycling. These structural and morphological characterizations confirm the phase purity and geometrical structures at nanoscale of the synthesized cathode material.

### 2.5. Electrochemical Measurement

The fabricated Fe-ion coin cell CR2023 under went several electrochemical measurements in the 2-electrode system, where CA is a working electrode and mild steel is a counter and reference electrode. CV was performed using the PalmSens MultiEmStat4 system in a 0.2–2.2 V potential window at 1–5 mV s<sup>-1</sup>. The Metrohm AUTOLAB PGSTAT302N is used for EIS before and after the GCD measurements. The Neware Battery Testing System (5V and 50 mA or 5V and 100 mA) is used to perform all the charge-discharge analyses at various current densities.

## 3. Results and Discussion

### 3.1. Structural and Morphological Characterization

The physical characterization of porous matrix carbon structures, exemplified by CAs, is pivotal in understanding their unique properties and potential role in working as a positive electrode for

Fe-ion batteries. We explored CA's intricate structural and morphological features using advanced analytical techniques such as FESEM, transmission electron microscopy (TEM), XRD, and BET surface area analysis. This comprehensive characterization unveils valuable insights into their nanoarchitecture, crystalline structure, and surface area, laying the groundwork for harnessing their full potential to help us understand the electrochemistry and participation in the mechanism of the Fe-ion battery.

Figure 2a shows the CA's spherical morphology with a diameter ranging from 2 to 10  $\mu\text{m}$  where pores are embedded into spheres, which has been confirmed from TEM. The XRD pattern of the synthesized CA is shown in Figure 2b. The graphitic cum amorphous nature of the synthesized CA can be easily noticed from the broad peaks corresponding to plane (002) and (100).<sup>[58]</sup> Figure 2c shows TEM images, confirming the CA's porous nature. The inset figure reveals the regular arrangement of nanopores. The substantial average pore size found by BET analysis matches the TEM images' average pore size distribution. The integrated pores inside the spherical particles help to improve the storage of the  $\text{Fe}^{2+}$  ions during charge–discharge. The controlled distribution of pore diameters significantly impacts the cathode electrode's stability and performance. BET measurements suggest the microporous structure of CA, exhibiting a large surface area of  $574.185 \text{ m}^2 \text{ g}^{-1}$  with  $0.3109 \text{ cc g}^{-1}$  pore volume and  $\approx 2 \text{ nm}$  pore size after nitrogen adsorption, as shown in Figure 2d. The pore size results are consistent with the TEM results. The larger specific capacity of the fabricated battery can be attributable to the substantial increase in the active surface area of CA. The high surface area and pore volume can be related to  $\text{Fe}^{2+}$  ions intercalation and deintercalation, which is further confirmed by the CV analysis, as discussed in the next section, where CA helps in the

diffusion-controlled process rather than the capacitive-controlled process during the cycling.

Figure 2e shows the FESEM image of the mild steel after cleaning with fine sandpaper. The lined structure can easily be seen on the surface of the mild steel, which is the imprint originating at the time of cleaning with fine sandpaper. The mild steel XRD contains three significant peaks at  $2\theta$  of  $\approx 44.78^\circ$ ,  $\approx 65^\circ$ , and  $\approx 82.38^\circ$ , which correspond to (110), (200), and (211) diffraction planes, respectively, as shown in Figure 2f. All these peaks are consistent with #ICDD JCPDS 85–1526 and thus, substantiate the BCC crystal structure of Fe.

### 3.2. CV Analysis

CV analysis is essential for analyzing the cathode materials' redox properties at various scan rates. Fig. S3 represents the electroplating/stripping process of the  $\text{Fe}^{2+}$  ion during the CV at  $10 \text{ mV s}^{-1}$ , which shows the plating or stripping of  $\text{Fe}^{2+}$  ions at mild steel using platinum as a counter, mild steel as a reference, and copper as the working electrode. A detailed charge–discharge mechanism for the CA cathode material is shown in Figure 3a, along with the complete schematic of the Fe-ion batteries with cathode, anode, and a nonaqueous electrolyte. Where CA works as the cathode material for storing  $\text{Fe}^{2+}$  ions during cycling,  $\text{Fe}^{2+}$  ions move between the anode and the cathode through the electrolyte. During the charging process,  $\text{Fe}^{2+}$  ions and electrons migrate from the cathode to the anode via the electrolyte and external circuit, respectively. In the discharging, the process will be exactly reversible of the charging process. CV was investigated to analyze the exact process of the  $\text{Fe}^{2+}$  ions storage mechanism. Figure 3b

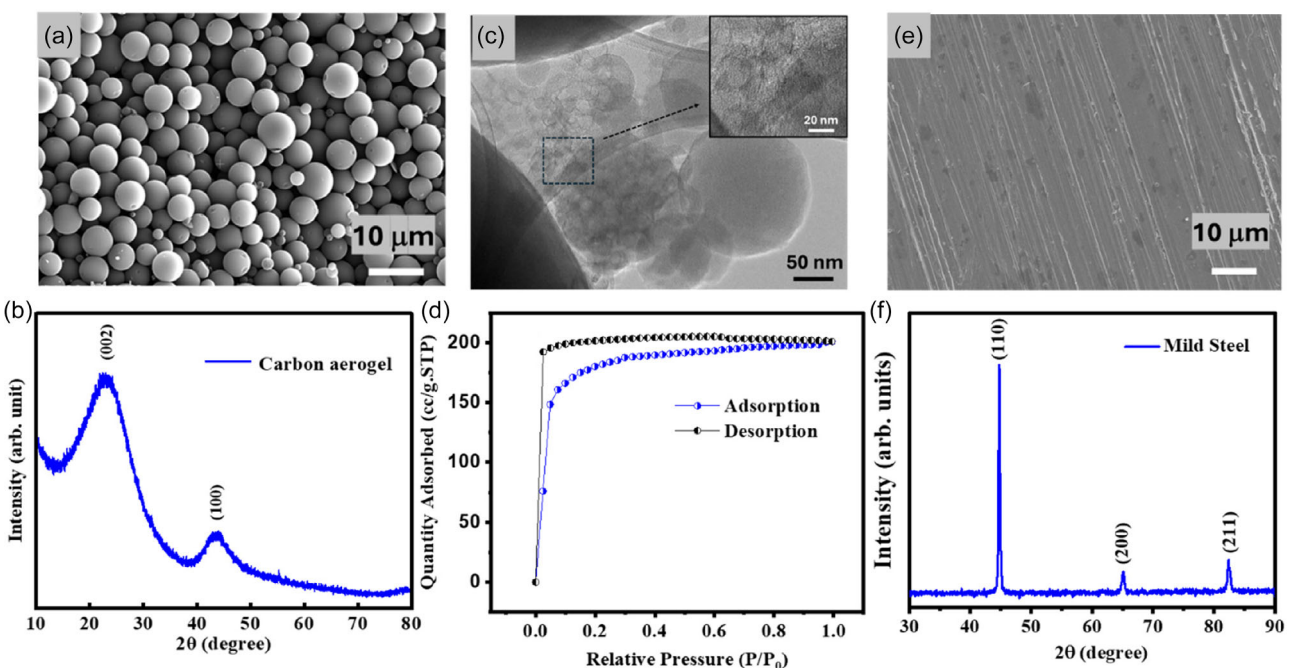


**Figure 2.** a) FESEM image of CA, b) XRD pattern of CA, c) TEM images of the CA with magnified porosity picture, d)  $\text{N}_2$  adsorption isotherms curve quantity absorbed versus relative pressure for CA, e) FESEM image of mild steel, f) XRD pattern of mild steel.

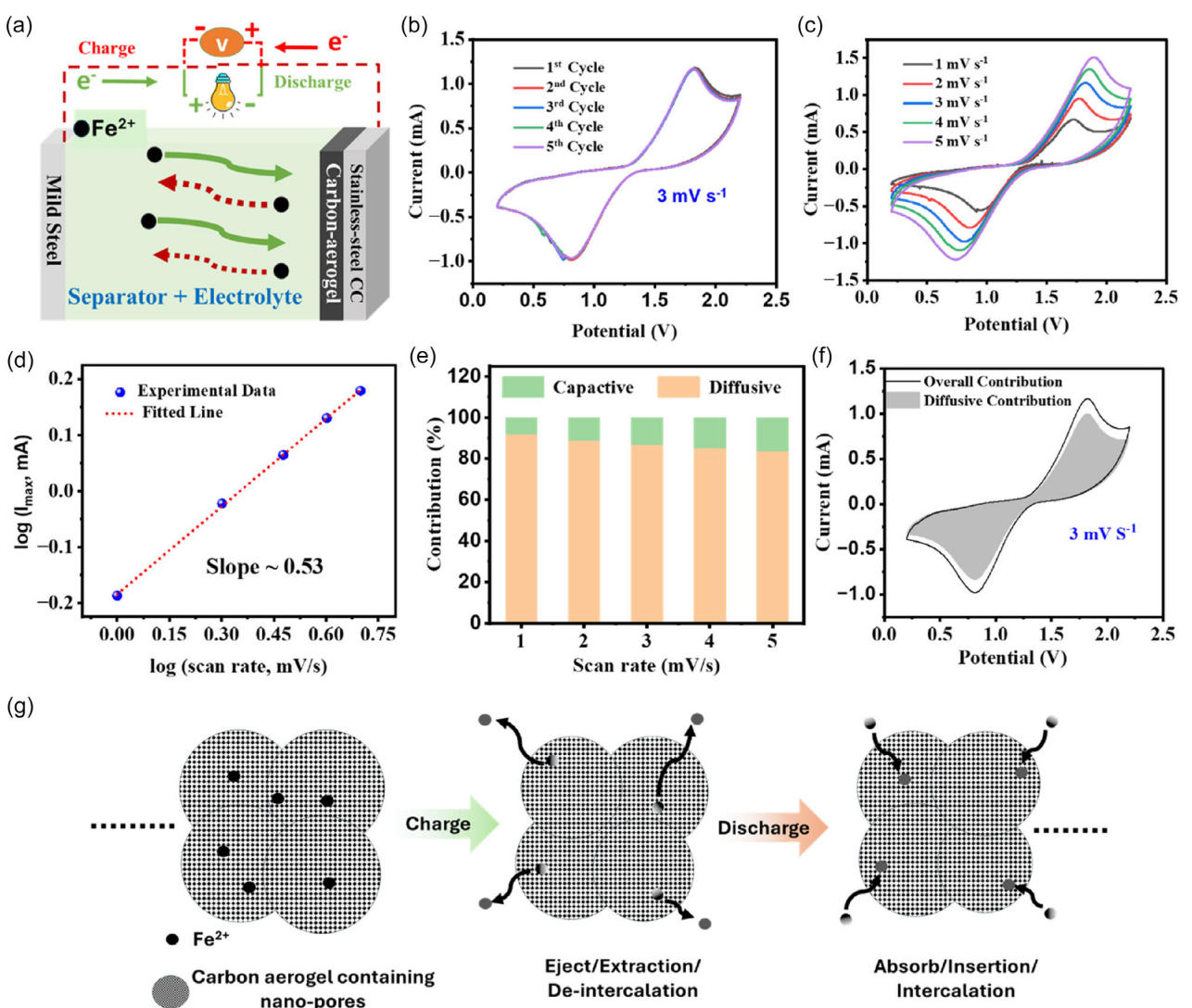


**Figure 3.** a) Charge–discharge mechanism for CA cathode of Fe-ion batteries, b) CV at  $3 \text{ mV s}^{-1}$  for starting five cycles, c) CV plot at starting cycle for various scan rates, d) plot for the log function of scan rate versus  $i_{\max}$ , e) percentage contribution with scan rate, f) CV plot difference for diffusive versus overall contribution at  $3 \text{ mV s}^{-1}$ , g) proposed charge–discharge mechanism by CA cathode.

shows the CV plot for the starting five cycles at  $3 \text{ mV s}^{-1}$  with an oxidation at  $\approx 1.81 \text{ V}$  and a reduction peak at  $\approx 0.80 \text{ V}$ , also CV plots entirely overlap, which indicates a reversible mechanism for the  $\text{Fe}^{2+}$  ion storage by the CA cathode during the multiple scans. Further, CV measurements were carried out at the various scan rates from  $1 \text{ mV s}^{-1}$  to  $5 \text{ mV s}^{-1}$  to evaluate the exact phenomena of  $\text{Fe}^{2+}$  ions storage mechanism in the CA cathode. These measurements are shown in Figure 3c. The position of the oxidation and the reduction peak uniformly varied with the higher scan rate, higher potential, and lower potential, respectively. The power law as described by the (Equation 1) was used to determine the charge storage mechanism process via active cathode materials as ( $i_{\max}$  = peak current and  $v$  = scan rate). It can also be expressed as (Equation 2)

$$i_{\max} = a \cdot v^b \quad (1)$$

$$\log(i_{\max}) = \log a + b \cdot \log(v) \quad (2)$$

where the value of the  $b$  is the slope between the  $\log(i_{\max})$  versus  $\log(v)$ .<sup>[41]</sup> The data is plotted between the  $\log(i_{\max})$  versus  $\log(v)$  and fitted with a straight line, as shown in Figure 3d. The value of  $b$  is  $\approx 0.53$ , which is close to 0.5, substantiating that the diffusion-controlled process mainly governs the  $\text{Fe}^{2+}$  ions storage mechanism. Further exact contributions of the capacitive and diffusion-controlled process are calculated for the CA cathode using the (Equation 3)

$$i_{\max} = k_1 \cdot v + k_2 \cdot v^{1/2} \quad (3)$$

where the  $k_1 v$  corresponds to a capacitive-controlled process and the  $k_2 v^{1/2}$  corresponds to a diffusive-controlled process.<sup>[59]</sup> The contribution of the diffusive-controlled process is 91.93%, 88.96%, 86.80%, 85.07%, and 83.59% at the scan rate of 1, 2, 3, 4,  $5 \text{ mV s}^{-1}$ , respectively. It shows that the diffusive percentage decreases with increasing scan rates, and a respective increase in the capacitive-controlled process with increasing scan rates, as

shown in Figure 3e. The percentage contribution is also plotted via CV diagram at  $3 \text{ mV s}^{-1}$  as shown in Figure 3f, where a black curve shows the overall contribution and diffusive-controlled process by brown filled color. These findings indicate that the CA cathode is more suitable for diffusive than capacitive-controlled processes due to its unique properties, including high surface area and pore volume, which provide an easy intercalation (insertion)/de-intercalation (extraction) path for  $\text{Fe}^{2+}$  ions. According to the physical characterization and CV analysis, we proposed the charge–discharge mechanism of the IIBs based on the CA cathode. As we discussed, the CA contains nanopores that help absorb/insert/intercalate or eject/extract/de-intercalation the Fe-ions during the charge–discharge, as illustrated in Figure 3g.

### 3.3. GCD Analysis

The GCD measurements are carried out to analyze the specific discharge capacity, CE, discharge voltage plateau, and rate capability at the various current densities for the CA Fe-ion coin cells. The specific capacity (in  $\text{mAh g}^{-1}$ ) was calculated as shown in the formula in (Equation 4), where  $I$  is the charge or discharge current in  $\text{mA}$ ,  $t$  time in hours, and  $m$  is the mass grams. The coin cell is

tested at higher and lower current rates to analyze the specific capacity. The cell shows the specific capacity of  $\approx 150$  and  $\approx 45 \text{ mAh g}^{-1}$  at  $35 \text{ mA g}^{-1}$  and  $1000 \text{ mA g}^{-1}$ , respectively. The cell also shows a discharge voltage plateau at  $\approx 0.85$ , as displayed in Figure 4a. The Fe-ion cell is cycled at various current densities from  $75 \text{ mA g}^{-1}$  to  $1000 \text{ mA g}^{-1}$ , and GCD data are plotted between the discharge capacity & CE with the cycles, where it shows the excellent capacity retention at numerous current densities, as revealed in Figure 4b. Initially, the cell is cycled at  $75 \text{ mA g}^{-1}$ , showing a capacity of  $\approx 100 \text{ mAh g}^{-1}$  with CE more than 60% in the starting 10 cycles. The cell was investigated at a higher current density of  $250 \text{ mA g}^{-1}$  to analyze the discharge capacity and CE, where it shows a capacity of  $\approx 70 \text{ mAh g}^{-1}$  with more than 80% of CE for the 10 cycles. Also, the cell is cycled at  $500$ ,  $750$ , and  $1000 \text{ mA g}^{-1}$  for 10 cycles at each current rate, showing more than 80% CE along with high-capacity retention. Finally, the cell is cycled again at  $75 \text{ mA g}^{-1}$  and  $250 \text{ mA g}^{-1}$ , showing similar discharge capacity and CE. Another cell is investigated at  $100 \text{ mA g}^{-1}$  for more than 40 cycles, showing 85% or more capacity stability, as illustrated in Figure 4c.

$$\text{Specific Capacity} = \frac{I \times t}{m} \quad (4)$$

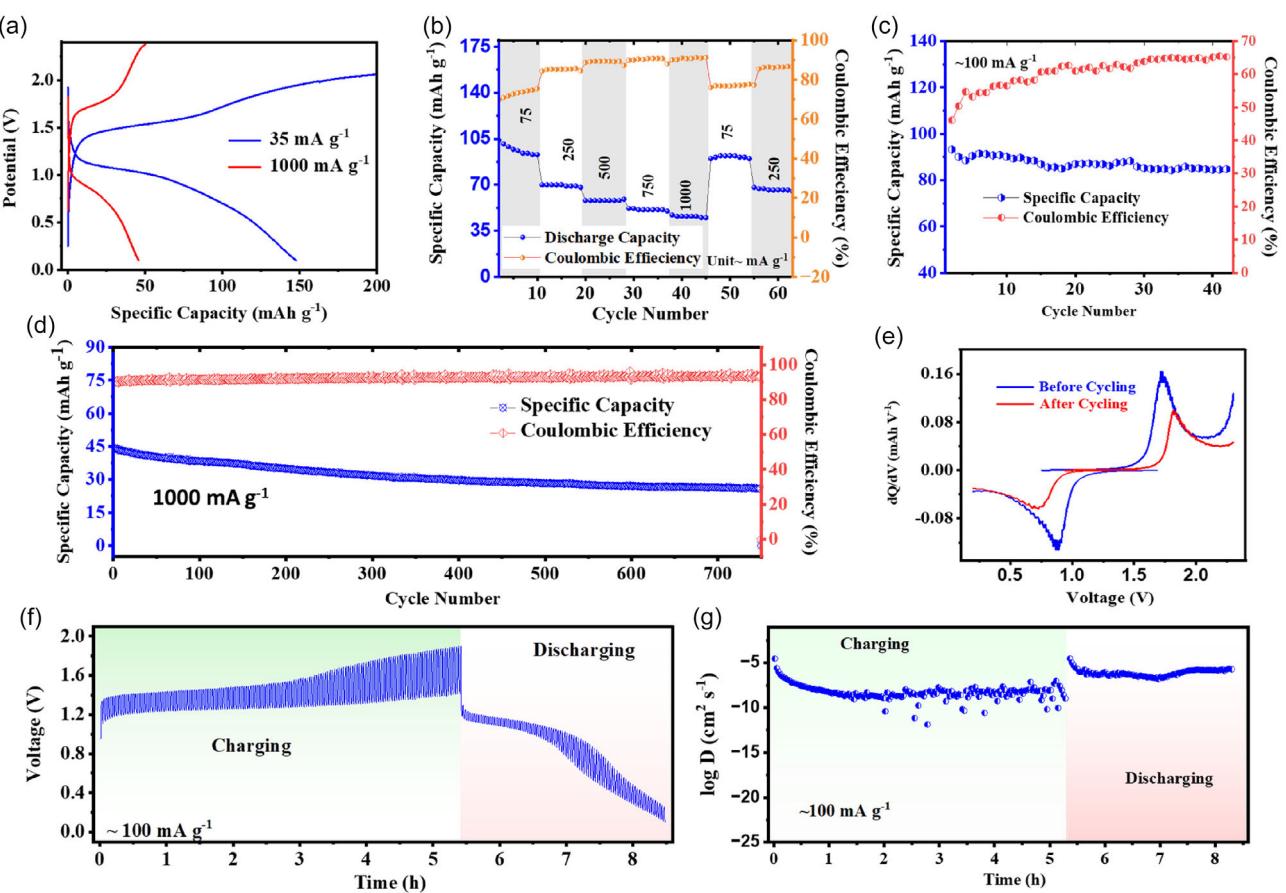


**Figure 4.** a) GCD curve at  $35$ ,  $1000 \text{ mA g}^{-1}$ , b) cyclic stability at various current densities, c) cyclic stability at  $100 \text{ mA g}^{-1}$  with cycle number, d) cyclic stability at high rate  $1000 \text{ mA g}^{-1}$ , e)  $dQ/dV$  plot with the voltage before and after GCD cycling, f) GITT charge–discharge curves at  $100 \text{ mA g}^{-1}$ , g) corresponding diffusion profile with time in charge–discharge.

Further, the cell is investigated at 1000 mA g<sup>-1</sup> to analyze capacity & rate capability. It shows the capacity retention of ≈60% along the CE of ≈85% in 750 cycles, as shown in Figure 4d. The GCD charge-discharge data is also plotted into the dQ/dV with the voltage before and after 750 cycles at 1000 mA g<sup>-1</sup>, as shown in Figure 4e. The dQ/dV versus voltage plot is similar to the CV, as discussed in the previous section, and these peaks indicate the intercalation/ deintercalation of the Fe<sup>2+</sup> ions via CA during cycling. The height and peak position of dQ/dV show a slight shift after the complete GCD cycling, which is also correlated with slight capacity degradation, as shown in Figure 4d. Further, galvanostatic intermittent titration technique was performed to analyze the diffusion profile of Fe<sup>2+</sup> ions into a carbon-based cathode for the iron-ion battery at 100 mA g<sup>-1</sup> using (Equation 5).

$$D = \left( \frac{4}{\pi \tau} \right) \left( \frac{m_B V_M}{M_B S} \right)^2 \left( \frac{\Delta E_s}{\Delta E_t} \right)^2 \quad (5)$$

Where  $D$  is the diffusion coefficient unit of cm<sup>2</sup> s<sup>-1</sup>,  $\tau$  represents the duration of the current pulse in seconds,  $m_B$  is the mass of the active material in grams,  $V_M$  is the molar volume,  $M_B$  is the molecular weight, and  $S$  is the surface area of the active material. The  $\Delta E_s$  is the steady-state voltage change (in V) observed after the relaxation period when the current is stopped; it represents the voltage difference between the initial equilibrium voltage before the pulse and the final equilibrium voltage after the relaxation period. The  $\Delta E_t$  represents the change in voltage V during the current pulse. It is the difference between the initial equilibrium voltage and the voltage at the end of the current pulse.<sup>[60,61]</sup> Figure 4f shows the charge-discharge plot for the GITT analysis. Corresponding to this, Figure 4g shows the diffusion coefficient profile, which suggests that the Fe<sup>2+</sup> ion is in the range  $3.11 \times 10^{-5}$ – $1.40 \times 10^{-12}$  cm<sup>2</sup> s<sup>-1</sup>. This high diffusion coefficient suggests that its nanopore CA network provides a high diffusion coefficient. The data regarding the voltage with time is also plotted, where the green curve corresponds to the charge and the red curve to the discharge at 1000 mA g<sup>-1</sup>. The complete single charge-discharge cycle takes an average of less than ≈7 min, showing fast charge-discharge behavior at a higher current rate, as shown in Figure 5a. The charge-discharge rate is almost equal to ≈18C rate, which shows the high-rate characteristics of the CA cathode for the rechargeable Fe-ion batteries. The unique characteristics of the nanopores make it a viable high-rate cathode for the Fe-ion batteries.

### 3.4. EIS Analysis and Demonstration

EIS offers detailed information on battery health and performance, aiding in diagnosing issues like electrode degradation and electrolyte behavior without disassembling the cell.<sup>[41,62,63]</sup> The EIS analysis is carried out before and after the GCD cycling (1000 mA g<sup>-1</sup>, 750 cycles) to interface resistance analysis with cycling and its correlation with capacity degradation. The EIS is done at the open circuit voltage in the 0.1 Hz to 10<sup>5</sup> Hz range. Figure 5b shows the Nyquist plot experimental data before

and after complete cycling. The Nyquist plot highlights the semi-circle's diameter, which has increased after cycling, indicating the higher SEI resistance after complete cycling. Further, these experimental data were fitted with the circuit model shown in Figure 5b and described mathematically in further equations. The observed and the fitted data are consistent with each other.

Where experimental data is fitted as the mentioned circuit with a combination of circuit elements to analyze the exact contribution of the impedance components based on resistor (R), capacitance (C), and constant phase element (CPE).<sup>[45]</sup> The fitted circuit was also mathematically expressed and simplified using various terms. The total impedance  $Z_{\text{total}}(\omega)$  of the iron-ion battery coin cell is modeled as the sum of three distinct contributions, as shown in (Equation 6) : bulk impedance ( $Z_b$ ) equal to bulk resistance ( $R_b$ ), solid electrolyte interphase layer impedance ( $Z_{\text{SEI}}$ ), and charge transfer impedance( $Z_{\text{ct}}$ ). The first term  $R_b$ , represents the bulk resistance arising from the electrolyte and internal cell components, including all the wire connections. The second term models the SEI layer as a parallel combination of a resistance ( $R_{\text{SEI}}$ ) and a capacitance ( $C_{\text{SEI}}$ ), which is related to ion transport resistance and charge accumulation at the electrode-electrolyte interface. The third term describes the charge transfer process at the electrode surface, incorporating a charge transfer resistance ( $R_{\text{ct}}$ ) in parallel with a series combination of a double-layer capacitance ( $C_{\text{dl}}$ ) and a constant phase element (CPE) characterized by parameters Q(Y0) and N, which account for nonidealities such as surface roughness and heterogeneity.<sup>[41,63,64]</sup> These components are mathematically elaborated, as shown in Eq. (7). The derived impedance expression correctly follows the fitted equivalent circuit shown in Figure 5b. Where the SEI branch ( $R_{\text{SEI}} \parallel C_{\text{SEI}}$ ) is in series with  $R_b$ , followed by the charge transfer branch ( $R_{\text{ct}} \parallel (C_{\text{dl}} - \text{CPE})$ ) in series. This model effectively represents the electrochemical behavior of the iron-ion battery, capturing both charge storage and reaction kinetics. Further, all the equations are simplified in the (Equation 8) and (Equation 9).

$$Z_{\text{total}}(\omega) = Z_b + Z_{\text{SEI}}(\omega) + Z_{\text{ct}}(\omega) \quad (6)$$

$$Z_{\text{total}}(\omega) = R_b + \left[ \frac{1}{R_{\text{SEI}}} + j\omega C_{\text{SEI}} \right]^{-1} + \left[ \frac{1}{R_{\text{ct}}} + \frac{1}{Z_{\text{dl-CPE}}} \right]^{-1} \quad (7)$$

$$Z_{\text{total}}(\omega) = R_b + \left[ \frac{1}{R_{\text{SEI}}} + j\omega C_{\text{SEI}} \right]^{-1} + \left[ \frac{1}{R_{\text{ct}}} + \frac{1}{\left( \frac{1}{j\omega C_{\text{dl}}} + \frac{1}{Q(j\omega)^N} \right)} \right]^{-1} \quad (8)$$

$$\begin{aligned} Z_{\text{total}}(\omega) = R_b + \frac{R_{\text{SEI}}}{1 + j\omega C_{\text{SEI}} R_{\text{SEI}}} \\ + \frac{R_{\text{ct}}[Q(j\omega)^N + j\omega C_{\text{dl}}]}{Q[Q(j\omega)^N + j\omega C_{\text{dl}}] + R_{\text{ct}} Q(j\omega)^{N+1} C_{\text{dl}}} \end{aligned} \quad (9)$$

Figure 5c shows the experimental and fitted data before the GCD cycling, along with the exact fitted circuit, with all the component values. Figure 5d shows the experimental and fitted data after the GCD cycling with the exact fitted component value. When both circuit was compared with the fitted circuit components, the fitted circuit results show a considerable change in the

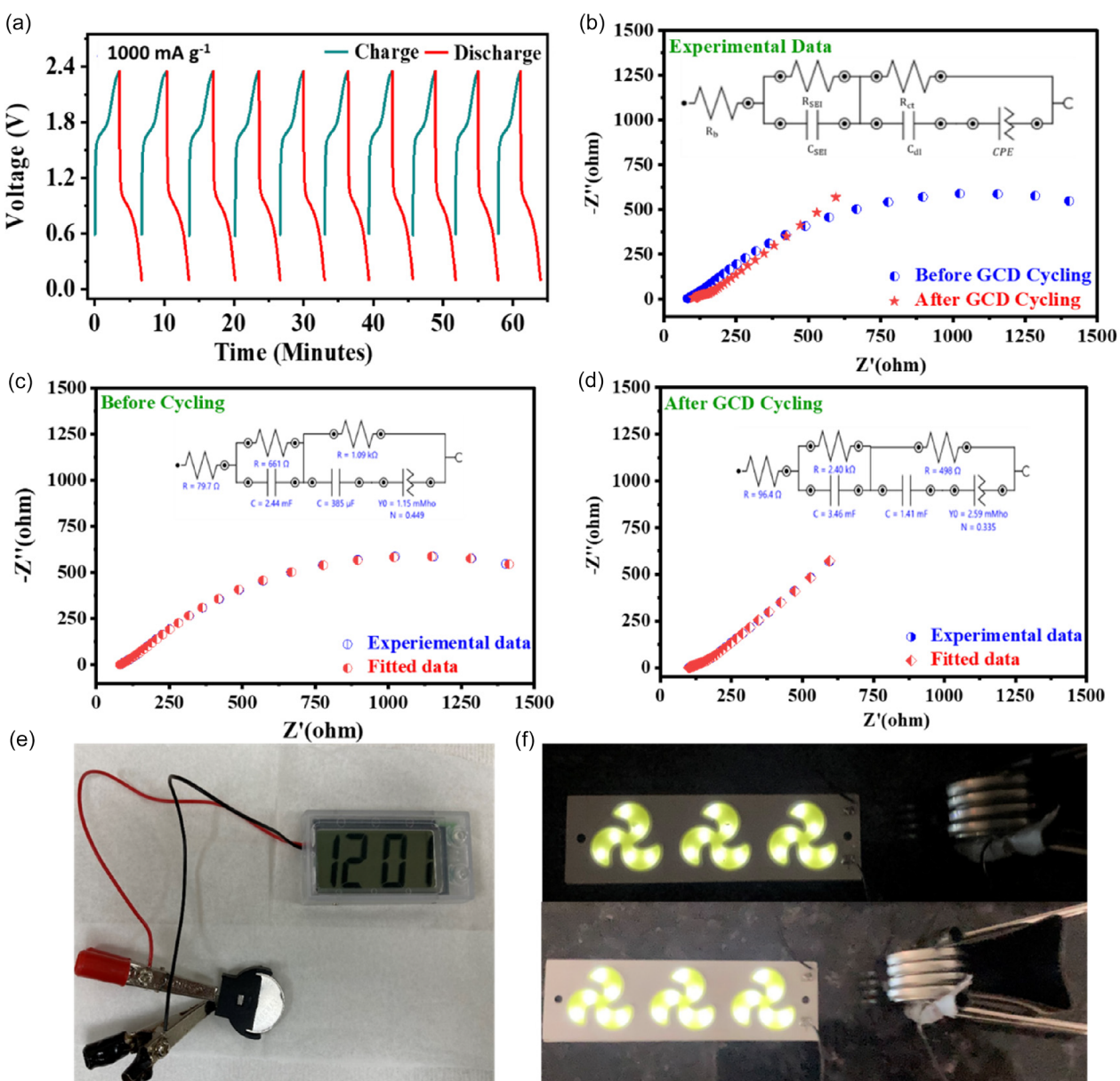


**Figure 5.** a) Voltage versus time plot, Nyquist plot. b) Experimental data before and after cycling with fitted model circuit, experimental data along fitted circuit data. c) Before cycling. d) After cycling. e) Demonstration of the digital clock using CA-based single Fe-ion coin cell. and f) 5V LEDs-based fan-shaped light unit using four coin cells in the series.

$R_{SEI}$  from 661 Ω to 2.4 kΩ, indicating the formation of the SEI during cycling. The  $R_b$  and  $R_{ct}$ , the resistance change, is negligible compared to the SEI resistance. The other components, including  $C_{SEI}$ ,  $C_{dl}$ , and CPE, also do not show significant changes. These results show that capacity degradation mainly arises due to the mostly SEI formation at the electrode surface, confirmed via postmortem analysis, as discussed in the next section.

Further, the demonstration was performed using various electronic gadgets to show CA's potential for the iron-ion battery. The single Fe-ion CR2032 coin cell is used to power the digital clock, as shown in Figure 5e. A 18 LEDs containing fan-shaped electronic gadget was switched on with four coin cells in series, as shown in Figure 5f, demonstrating the potential of Fe-ion batteries.

### 3.5. Electrode's Postmortem Analysis

The cell was opened after the GCD cycling (1000 mA g<sup>-1</sup>, 750 cycles) for the post-mortem analysis using the SEM and XRD analysis of the coated electrode. Figure 6a shows the SEM and EDAX picture of cathode-coated slurry on the SS before use in the coin cell. Where CA microspheres can be seen easily in the SEM picture, and EDAX confirms the presence of various elements, including C (carbon) as the main source, which contains almost 97.29 atomic weight percent, F contains an atomic weight percent of 2.71, coming from the binding agent. Figure 6a also shows the cathode's SEM and EDAX picture after the complete cycling. It contains C, Fe, F, O, and Cl in different atomic

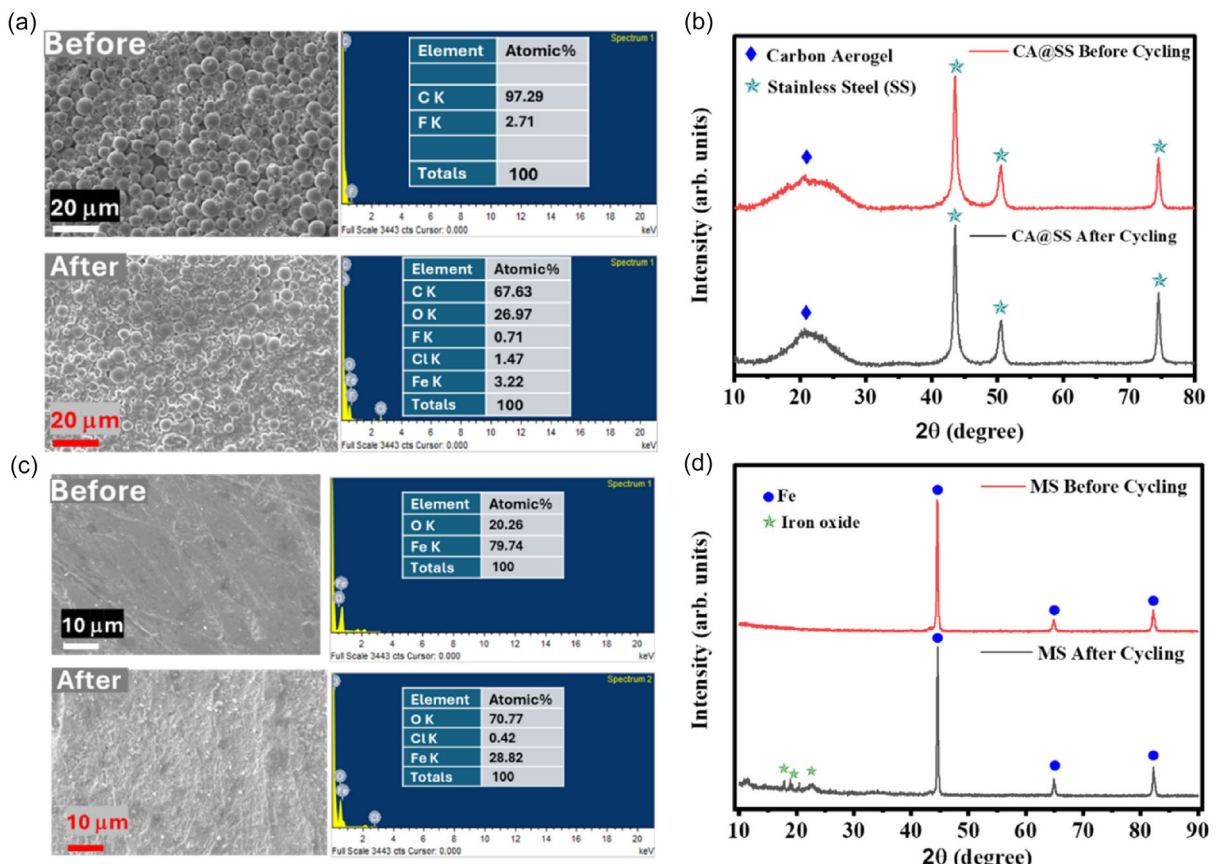


**Figure 6.** Before and after cycling a) SEM image with EDAX spectra of cathode, b) XRD spectra cathode coated on SS, c) SEM image with EDAX spectra of anode, d) XRD spectra of anode.

percentages due to its contact with the electrolyte during cycling, making a cathode–electrolyte interface. The morphology of the CA is spherical, as before the cycling, which shows the stability of the CA, but its looking joints are mostly due to the electrode–electrolyte interface. Similarly, XRD was also investigated before and after the GCD cycling. There are no changes in the XRD peaks before and after cycling, as shown in Figure 6b. The star symbols correspond to the SS peak due to their use as their current collector, and the rectangle symbol shows the CA peaks. The unchanged peaks show the stability of the CA cathode after the cycling.<sup>[45,58]</sup>

Figure 6c shows the SEM and EDAX pictures of cleaned mild steel before use in the coin cell, which contains a plane surface with a lined structure due to sandpaper polishing. The EDAX mapping shows MS contains around ≈79.24 atomic percentage of Fe, with the rest as oxygen. After the GCD cycling, a layer was formed on the MS's surface, as shown in Figure 6c. EDAX mapping shows the atomic percent of oxygen increases up to ≈71%, indicating the oxide layer formation at the surface of the MS during the cycling. Similarly, XRD was also investigated before and after the GCD cycling. After the cycling, additional peaks are available, representing the mixed iron oxide with a star symbol at the

**Table 1.** Electrochemical performance comparison of various reported cathodes for rechargeable Fe-ion batteries based on the nonaqueous electrolyte.

S.No.	Positive electrode	Negative electrode	Nonaqueous Electrolyte	Synthesis conditions	Highest discharge capacity [mAh g <sup>-1</sup> ] at current density [mA g <sup>-1</sup> ]	Capacity retention [%] in cycle number at current density [mA g <sup>-1</sup> ]	Ref.
1	Bulk V <sub>2</sub> O <sub>5</sub>	MS	1M Iron-perchlorate	Inert	207 at 30	54% in 50 cycles at 30	[44]
2	g-C <sub>3</sub> N <sub>4</sub>	MS	1M Iron-perchlorate	Ambient	130 at 40	≈60% in 240 cycles at 400	[45]
3	V <sub>2</sub> O <sub>5</sub>	MS	1M Iron-perchlorate	Ambient	120 at 33	50% in 30 cycles at 30	[41]
4	C/Fe, C/Fe <sub>2</sub> O <sub>3</sub>	Graphite	BmimFeCl <sub>4</sub> ionic liquid	Inert	100	–	[65]
5	V <sub>2</sub> O <sub>5</sub> Microspheres	MS	1M Iron-perchlorate	Ambient	205 at 33	70% in 600 cycles at 3000	[66]
6	Fe <sub>3</sub> O <sub>4</sub> Microspheres	MS	1M Iron-perchlorate	Ambient	155 at 25	92% in 500 cycles at 500	[67]
7	Carbon aerogel	MS	1M Iron-perchlorate	Ambient	≈150 at 35	≈60% in 750 cycles at 1000	This work

surface of the mild steel during cycling with Fe denoted by the circle, as shown in Figure 6d. As discussed in the previous section, SEI's resistance is high after cycling, indicating an oxide layer formation at the anode, an iron oxide layer after cycling, combined verified by the SEM, EDAX, and XRD.<sup>[45]</sup> All the results are consistent with the EIS, contributing to the overall slight capacity degradation of the rechargeable Fe-ion batteries based on CA cathode materials.

**Table 1** presents a detailed comparison of the electrochemical performance of CA cathodes with various other reported cathode materials in nonaqueous iron-ion battery systems. The comparison highlights key parameters such as specific capacity, cycling stability, and rate capability, enabling a clear evaluation of the advantages and limitations of each material. Notably, the CA demonstrates competitive or superior performance in terms of specific capacity and cycle retention, indicating its potential as a promising cathode material for high-performance nonaqueous rechargeable IIBs.

## 4. Conclusions

In summary, CA is synthesized via the sol-gel technique followed by carbonization, which offers unique properties, making it suitable for the cathode materials for Fe-ion batteries. CV is investigated at different scan rates to analyze the redox mechanism, suggesting that aerogel is more dominant by the diffusion-controlled process. The GCD characteristics showed high specific capacities of  $\approx 150$  and  $\approx 45 \text{ mAh g}^{-1}$  at  $35 \text{ mA g}^{-1}$  and  $1000 \text{ mA g}^{-1}$  current densities, respectively. The capacity retention is over 60% in 750 cycles at  $1000 \text{ mA g}^{-1}$  with fast charge-discharge characteristics of  $\approx 18\text{C}$  rate. EIS and postmortem measurements showed that SEI formation is the primary source of observed capacity degradation, consistent with the GCD results. Thus, the present work explains that CA can be an efficient cathode material for IIBs with enhanced electrochemical performance.

## Acknowledgments

A.D is thankful to ANRF (previously SERB), DST, Government of India, for carrying out this work under projects #CRG/2020/004023 & #SERB/F/10090/2021–2022. Authors also acknowledge AloT Fab Facility and CRF, IIT Jodhpur, for providing support for physical characterizations. Author Jitendra K Yadav thanks the A-MAD Research Group members for their technical assistance throughout the work.

## Conflicts of Interest

The authors declares no conflicts of interest.

## Data Availability Statement

The data that support the findings of this study are available in the supplementary material of this article.

**Keywords:** carbon aerogel cathode • galvanostatic intermittent titration technique analysis • impedance analysis • iron-ion batteries • mild steel anode

- [1] T. A. Faunce, J. Prest, D. Su, S. J. Hearne, F. Iacopi, *MRS Energy Sustain.* **2018**, *5*, 10.
- [2] M. Kumar, B. Meena, P. Subramanyam, D. Suryakala, C. Subrahmanyam, *Catalysts* **2022**, *12*, 1198.
- [3] R. Sharma, H. Kumar, G. Kumar, S. Sharma, R. Aneja, A. K. Sharma, R. Kumar, P. Kumar, *Chem. Eng. J.* **2023**, *468*, 143706.
- [4] M. Yadav, J. K. Yadav, S. Choudhari, P. Kumar, P. Ram, *J. Indian Chem. Soc.* **2025**, *102*, 101529.
- [5] J. B. Goodenough, *J. Solid State Electrochem.* **2012**, *16*, 2019.
- [6] H. Gupta, M. Kumar, D. Sarkar, P. W. Menezes, *Energy Adv.* **2023**, *2*, 1263.
- [7] A. P. Pandey, J. K. Yadav, A. Dixit, *Royal Soc. Chem.* **2025**, *3*, 318.
- [8] A. Kumar, P. Bashiri, B. P. Mandal, K. S. Dhindsa, K. Bazzi, A. Dixit, M. Nazri, Z. Zhou, V. K. Garg, A. C. Oliveira, P. P. Vaishnavi, V. M. Naik, G. A. Nazri, R. Naik, *Inorganics* **2017**, *5*, 67. <https://doi.org/10.3390/inorganics5040067>.
- [9] J. U. Choi, N. Voronina, Y. K. Sun, S. T. Myung, *Adv Energy Mater* **2020**, *10*, 1.
- [10] N. Mohamed, N. K. Allam, *RSC Adv.* **2020**, *10*, 21662.
- [11] J. K. Yadav, A. Dixit, *Royal Soc. Chem.* **2025**, *3*, 23, <https://doi.org/10.1039/9781837673612-00023>.
- [12] C. M. Julien, A. Mauger, K. Zaghib, H. Grout, *Inorg. Basel* **2014**, *2*, 132.
- [13] M. Shahjalal, P. K. Roy, T. Shams, A. Fly, J. I. Chowdhury, M. R. Ahmed, K. Liu, *Energy* **2022**, *241*, 122881.
- [14] J. Xu, F. Xie, L. Huang, N. Li, S. Peng, W. Ma, K. Zhang, Y. Wu, L. Shao, X. Shi, J. Chen, L. Tao, K. Zhang, Z. Zhang, Y. Wang, Z. Sun, *Nat. Commun.* **2025**, *16*, 4977.
- [15] B. Rani, J. K. Yadav, P. Saini, A. Dixit, *Sustain Energy Fuels* **2025**, *9*, 4262.
- [16] X. Nie, Z. Chen, B. Deng, L. Shao, J. Xu, X. Shi, Z. Sun, *Adv. Energy Mater.* **2025**, *15*, 2500069.
- [17] C. Shi, D. Muhtar, X. Lu, F. Liu, X. Lu, Z. Sun, Z. Guo, *Adv. Energy Mater.* **2025**, *15*, 2500448.
- [18] M. Gu, S. Chen, J. Xu, X. Shi, L. Shao, Z. Sun, *ACS Appl. Mater. Interf.* **2025**, *17*, 22546.
- [19] J. Y. Hwang, S. T. Myung, Y. K. Sun, *Chem. Soc. Rev.* **2017**, *46*, 3529.
- [20] P. K. Nayak, L. Yang, W. Brehm, P. Adelhelm, *Angewandte Chemie Int. Ed.* **2018**, *57*, 102.
- [21] M. A. Schroeder, L. Ma, G. Pastel, K. Xu, *Curr. Opin. Electrochem.* **2021**, *29*, 100819.
- [22] Y. Liang, H. Dong, D. Aurbach, Y. Yao, *Nat. Energy* **2020**, *5*, 646.
- [23] Y. Hu, C. Fu, S. Chai, Q. He, Y. Wang, M. Feng, Y. Zhang, A. Pan, *Adv. Powder Mater.* **2023**, *2*, 100093.
- [24] Y. Yang, L. Qin, Q. He, C. Yin, Y. Lei, S. Liang, G. Fang, *Sci. Bull. Beijing* **2025**, *70*, 104.
- [25] X. Zhang, R. Lv, W. Tang, G. Li, A. Wang, A. Dong, X. Liu, J. Luo, *Challenges Adv. Funct. Mater.* **2020**, *30*, 1.
- [26] Y. Yang, H. Yang, X. Wang, Y. Bai, C. Wu, *J. Energy Chem.* **2022**, *64*, 144.
- [27] G. A. Elia, N. A. Kyeremateng, K. Marquardt, R. Hahn, B. Supercaps, **2019**, *2*, 83.
- [28] N. Huang, C. Yao, J. Cheng, F. Yu, Y. Zhao, F. Li, Y. Ou, L. Liu, *Next Mater.* **2024**, *4*, 10022.
- [29] H. Sun, W. Wang, Z. Yu, Y. Yuan, S. Wang, S. Jiao, *Chem. Commun.* **2015**, *51*, 11892.
- [30] N. Ma, P. Wu, Y. Wu, D. Jiang, G. Lei, *Funct. Mater. Lett.* **2019**, *12*, 1.
- [31] Q. Guo, W. Zeng, S. L. Liu, Y. Q. Li, J. Y. Xu, J. X. Wang, Y. Wang, *Rare Metals* **2021**, *40*, 290.
- [32] B. Rani, J. K. Yadav, P. Saini, A. P. Pandey, A. Dixit, *Energy Storage* **2024**, *6*, e586.
- [33] J. K. Yadav, B. Rani, P. Saini, A. Dixit, *Energy Adv.* **2024**, *3*, 927.
- [34] Z. He, F. Xiong, S. Tan, X. Yao, C. Zhang, Q. An, *Mater. Today Adv.* **2021**, *11*, 100156.
- [35] S. K. Sandstrom, X. Ji, *ACS Cent. Sci.* **2022**, *8*, 686.
- [36] J. Liu, D. Dong, A. L. Caro, N. S. Andreas, Z. Li, Y. Qin, D. Bedrov, T. Gao, *ACS Cent. Sci.* **2022**, *8*, 729.
- [37] H. Lv, Z. Wei, C. Han, X. Yang, Z. Tang, Y. Zhang, C. Zhi, H. Li, *Nat. Commun.* **2023**, *14*, 3117.
- [38] X. Wu, A. Markir, Y. Xu, E. C. Hu, K. T. Dai, C. Zhang, W. Shin, D. P. Leonard, K. Kim, X. Ji, *Adv. Energy Mater.* **2019**, *9*, 1.
- [39] S. N. Jagadeesan, F. Guo, R. T. Pidathala, A. M. M. Abeykoon, G. Kwon, D. Olds, B. Narayanan, X. Teng, *ChemSusChem* **2024**, *17*, e20240050.

- [40] C. Li, X. Guo, W. Deng, N. Shen, Y. Zhou, Y. Chen, R. Li, *Small* **2024**, *20*, 2407715.
- [41] J. K. Yadav, B. Rani, A. Dixit, I. Kiel, *2023*, *29*, 1497.
- [42] X. Wu, A. Markir, Y. Xu, C. Zhang, D. P. Leonard, W. Shin, X. Ji, *Adv. Funct. Mater.* **2019**, *29*, 1.
- [43] Y. Xu, X. Wu, S. K. Sandstrom, J. J. Hong, H. Jiang, X. Chen, X. Ji, *Adv. Mater.* **2021**, *33*, 2105234.
- [44] A. P. V. K. Saroja, S. S. Samantaray, R. Sundara, S. Ramaprabhu, S. A.P.V., S. S. Samantaray, A. P. V. K. Saroja, S. S. Samantaray, R. Sundara, *Chem. Commun.* **2019**, *55*, 10416.
- [45] J. K. Yadav, B. Rani, A. Dixit, *J. Power Sour.* **2023**, *567*, 232943.
- [46] X. Guo, C. Li, W. Deng, Y. Zhou, Y. Chen, Y. Xu, R. Li, *Chin. Chem. Lett.* **2024**, *36*, 109715.
- [47] W. Wu, X. Yang, K. Wang, C. Li, X. Zhang, H. Y. Shi, X. X. Liu, X. Sun, *Chem. Eng. J.* **2022**, *432*, 134389.
- [48] Y. Zhang, Y. Tian, Z. Wang, C. Wei, C. Liu, Y. An, B. Xi, S. Xiong, J. Feng, *Chem. Eng. J.* **2023**, *458*, 141388.
- [49] C. Li, Y. Xu, W. Deng, Y. Zhou, X. Guo, Y. Chen, R. Li, *Small* **2023**, *20*, 2305766.
- [50] H. K. Hassan, A. Galal, N. F. Atta, T. Jacob, *J Alloys Compd.* **2021**, *870*, 159383.
- [51] C. Li, Y. Xu, W. Deng, N. Shen, Y. Chen, C. Huang, J. Zhu, R. Zhu, W. Zou, R. Li, *J. Power Sour.* **2023**, *581*, 233506.
- [52] G. Huang, Z. Lao, Z. He, F. Xiong, S. Tan, M. Huang, G. Thompson, Q. An, L. Mai, *Chem. Commun.* **2023**, *59*, 4067.
- [53] S. Sun, Q. Yan, M. Wu, X. Zhao, *Sustain. Mater. Technol.* **2021**, *30*, e00342.
- [54] S. Chai, J. Zhu, J. Jiang, C. M. Li, *Nano Res.* **2022**, *15*, 3187.
- [55] C. Bai, H. Jin, Z. Gong, X. Liu, Z. Yuan, *Energy Storage Mater.* **2020**, *28*, 247.
- [56] A. P. Pandey, M. A. Shaz, V. Sekkar, R. S. Tiwari, *Int J Hydrogen Energy* **2023**, *48*, 21404.
- [57] A. P. Pandey, A. Bhatnagar, V. Shukla, P. K. Soni, S. Singh, S. K. Verma, M. Shaneeth, V. Sekkar, O. N. Srivastava, *Int. J. Hydrogen Energy* **2020**, *45*, 30818.
- [58] A. P. Pandey, B. Rani, M. Sharma, J. K. Yadav, P. Saini, A. D. Shalu, *Energy Storage* **2023**, *6*, e549.
- [59] P. De, J. Halder, S. Priya, A. K. Srivastava, A. Chandra, *ACS Appl. Energy Mater.* **2022**, *6*, 753.
- [60] J. Kim, S. Park, S. Hwang, W.-S. Yoon, *J. Electrochem. Sci. Technol.* **2022**, *13*, 19.
- [61] Y. S. Xu, C. Li, W. J. Deng, J. L. Zhu, Y. Zhou, R. D. Zhu, C. Huang, W. X. Zou, R. Li, *Chem. Commun.* **2023**, *59*, 8576.
- [62] W. Choi, H. C. Shin, J. M. Kim, J. Y. Choi, W. S. Yoon, *J. Electrochem. Sci. Technol.* **2020**, *11*, 1.
- [63] U. Westerhoff, K. Kurbach, F. Liebesch, M. Kurrat, *Energy Technol.* **2016**, *4*, 1620.
- [64] E. Locorotondo, L. Pugi, L. Berzi, M. Pierini, S. Scavuzzo, A. Ferraris, A. G. Airale, M. Carello, in *5th International Forum on Research and Technologies for Society and Industry: Innovation to Shape the Future*, **2019**, 225.
- [65] Y. Zhao, Y. Zhen, T. Boström, T. Bostrom, *ACS Omega* **2022**, *7*, 24082.
- [66] J. K. Yadav, B. Rani, P. Saini, A. Dixit, *Energy Technol.* **2024**, *12*, 2401334.
- [67] J. K. Yadav, B. Rani, P. Saini, A. P. Pandey, A. Dixit, *Sustain. Energy Fuels* **2024**, *8*, 4617.

---

 Manuscript received: May 9, 2025

Revised manuscript received: August 15, 2025

Version of record online: